

Competing decay-channel fluorescence, dissociation, and ionization in superexcited levels of H₂M. Glass-Maujean,¹ Ch. Jungen,^{2,3} G. Reichardt,⁴ A. Balzer,⁴ H. Schmoranzner,⁵ A. Ehresmann,⁶ I. Haar,⁶ and P. Reiss⁶¹*Laboratoire de Physique Moléculaire pour l'Atmosphère et l'Astrophysique, Université Pierre et Marie Curie, 4 place Jussieu, F-75252 Paris Cedex 5, France*²*Laboratoire Aimé Cotton, Centre National de la Recherche Scientifique, Bâtiment 505, Université de Paris-Sud, F-91405 Orsay, France*³*Department of Physics and Astronomy, University College London, London WC1E 6BT, United Kingdom*⁴*BESSY II, Albert-Einstein-Strasse 15, D-12489 Berlin, Germany*⁵*Fachbereich Physik, Technische Universität Kaiserslautern, D-67653 Kaiserslautern, Germany*⁶*Institute of Physics and Interdisciplinary Nanostructure Science and Technology, Heinrich-Plett-Strasse 40, Universität Kassel, D-34132 Kassel, Germany*

(Received 21 October 2010; published 16 December 2010)

The absolute cross sections for the competing decay-channel fluorescence, dissociation, and ionization of photoexcited long-lived superexcited H₂ molecular levels have been measured from the ionization threshold of H₂ up to the H(1s) + H(*n* = 3) dissociation limit. The total and partial natural widths of these levels have been determined. Good agreement is found with first principles calculations carried out with the multichannel quantum defect theory for excited levels of ¹Π_u⁻ symmetry, which represent 70% of the levels studied experimentally. The calculations reproduce the balance between the competing decay processes as well as its substantial evolution from level to level.

DOI: [10.1103/PhysRevA.82.062511](https://doi.org/10.1103/PhysRevA.82.062511)

PACS number(s): 33.20.Wr, 33.50.Dq, 33.80.Eh, 33.80.Gj

I. INTRODUCTION

Molecular hydrogen H₂ is the most abundant molecule in the universe. With the advent of satellite-borne spectrometry its detection in astrophysical environments has become feasible. vuv emission spectra of H₂ are now known from the atmospheres of large planets [1] as well as from interstellar clouds [2]. Their interpretation requires detailed knowledge of both the spectroscopy and the decay dynamics. H₂ is a unique molecular system because it is the only molecule known to fluoresce when it is excited above the ionization and the dissociation thresholds [3].

In this paper we report detailed quantitative fluorescence, dissociation, and ionization yields for those superexcited molecular levels of H₂ which fluoresce. The experimental data presented here have been obtained at BESSY II in a synchrotron radiation experiment that has produced decay yields that are an order of magnitude more accurate than those measured previously [4]. The fact that we measure *absolute* absorption cross sections allows us to determine partial decay widths of superexcited levels even though the widths determined here are orders of magnitude smaller than the spectral resolution of the exciting photons. The experimental data are interpreted with the help of multichannel quantum defect theory (MQDT), which accounts simultaneously for the spectroscopic and the dynamical aspects of all 67 observed fluorescing ¹Π_u⁻ levels. The analogous theoretical treatment of the 12 observed fluorescing superexcited levels that have ¹Π_u⁺ and ¹Σ_u⁺ symmetry is deferred. Thirteen observed fluorescence lines remain unassigned at this time. A preliminary account of this work has been published previously [5].

II. EXPERIMENT

The experimental setup has been described in detail in previous publications [6–9]. The vuv photons coming from the undulator beam line U125/2-10m-NIM of BESSY II were

dispersed by a 10-m normal-incidence monochromator equipped with a 4800-line/mm grating giving a spectral resolution of 0.0010 nm at first order [10] (this value represents the convolution of the apparatus function with the Doppler width at room temperature). For comparison, the data presented in our preliminary communication [5] were obtained with a 1200-line/mm grating giving a resolution of 0.0012 nm at third order. The linearity of the monochromator's energy scale has been significantly improved by the Heydemann correction of the quadrature error of the angular encoder system that is used as feedback for the closed-loop drive of the monochromator [11]. The influence of the quadrature error on the spectroscopic data could be reduced below the vibrational and electronic noise level of the system. The uncertainty of the energies of the measured spectra has thus been improved significantly since the earlier publications [5–9,12], and it is typically ±1.0 to ±1.5 cm⁻¹. These numbers were obtained by comparison with published H₂ absorption spectra recorded on photographic plates [13–15]. The differences with respect to the recent Fourier transform measurements of Dickenson *et al.* [16] are somewhat smaller (≤1 cm⁻¹). The absorption and ionization excitation spectra were recorded at room temperature with a gas pressure of 20 mTorr, for a wavelength range extending from 81.0 to 74.0 nm, simultaneously with the Lyman-α fluorescence radiation from the H(*n* = 2) atomic fragments and the visible molecular fluorescence.

In order to eliminate any polarization effects, the L_α fluorescence emitted from the H(*n* = 2) fragments was detected by a microchannel plate (Hamamatsu F1552-01 Inconel) mounted at the magic angle with respect to the electric vector of the synchrotron radiation. A MgF₂ window placed in front of the detector was used to prevent charged particles from arriving on it. This window also absorbed the L_β fluorescence originating from H(*n* = 3) fragments as well as molecular fluorescence toward the X state which occurs below the MgF₂ cutoff. Further, the detector is not sensitive to visible and infrared radiation, so all molecular fluorescence is eliminated,

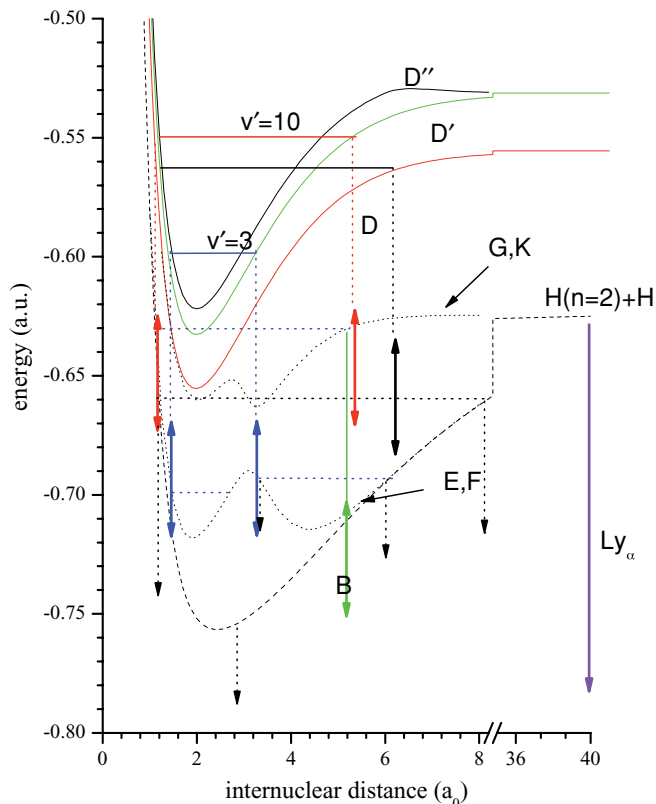


FIG. 1. (Color online) Selected potential energy curves for H_2 illustrating various photon emission pathways relevant in the present experiments. Double arrows correspond to the range of the accessible fluorescence window; see the text for details.

including the fluorescence terminating in the ground-state dissociation continuum. Photoions were collected by applying a voltage of 10 V to one of the two electrodes in the target cell.

The molecular fluorescence was detected in the wavelength range $350 \text{ nm} < \lambda < 700 \text{ nm}$, which corresponds to the sensitivity window of the photomultiplier (Photronics XP2258). The molecular fluorescence occurs predominantly in the vuv ($\lambda \approx 100 \text{ nm}$) since transitions toward the ground state are favored by the ν^3 frequency factor. Emission to the $EF^1\Sigma_g^+$ and $GK^1\Sigma_g^+$ states is also present. Depending on the vibronic levels involved in the transition, this emission may range from the infrared (not detected) to the visible spectral region where it is detected.

Figure 1 illustrates schematically which kinds of transitions will be observed within the detection window. Solid horizontal lines indicate examples of vibronic levels belonging to the $3p\pi D$, $4p\pi D'$, and $5p\pi D''$ states, respectively, which are excited by photoabsorption. Emission transitions from these upper levels corresponding to their classical turning points are indicated by dashed vertical lines that start from the emitting level. Vertical lines ending in an arrow represent transitions to the X ground state, which is not shown. The double-headed arrows represent the detection window and are placed corresponding to the energy of the upper level. The lower levels of these transitions belong to the *gerade* manifold of states and are depicted by horizontal dashed lines. It may be seen, for example, that the $4p\pi D', v = 3$ level

will preferentially emit toward the GK and EF (inner and outer wells) levels, but only the $4p\pi D' - EF$ emissions can actually be detected. The emission from the $4p\pi D', v = 10$ level is more complicated: the direct emission toward the GK vibronic levels can be observed, whereas the emission toward EF goes undetected. In addition *cascade* emission from GK to the $B^1\Sigma_u^+$ state is also detected. Note that L_α emission (also indicated in Fig. 1) originating from predissociated $\text{H}(n = 2)$ fragments is always outside the visible detection window.

The intensities of the absorption spectrum have been calibrated directly, based on the known gas pressure and the absorption path length. As a check, certain points have been recorded without gas at the beginning and at the end of the scanning procedure. The sources of uncertainty of the absolute cross-section measurements are the following: (i) the error of the pressure measurement (1%), (ii) the error of the temperature measurement (1%), (iii) the error of the determination of the effective path length, estimated by a calculation to be less than 5%, and (iv) the error of the determination of the detection efficiency of the transmitted light (1%). All these uncertainties add up to a total error of 6%, which has to be added to the statistical error due to the noise at each recorded point.

Both the L_α detection efficiency and the ion detection efficiency depend on the geometry and the detectors used, but they are independent of the wavelength of the exciting photon. We determined the L_α detection efficiency by comparing absorption and dissociation structures in the spectrum for lines that do not appear in the other channels so that it is certain that the dissociation yield is 100%. This is the case, for example, for the $D^1\Pi_u^+ - X^1\Sigma_g^+ R(1)$ transitions. The uncertainty of the dissociation yield thus obtained is estimated to be 5%, which has to be added to the error due to the noise at each recorded point. The ion detection efficiency was obtained from the comparison of the absorption and ionization structures of the spectrum at wavelengths where it is known that the ionization yield is 100%. The calibration uncertainty is again estimated to be 5%.

In principle, the efficiency of fluorescence detection may vary greatly from one level to another, for example, depending on the presence or absence of detectable cascade emission, as discussed. Therefore, the fluorescence signal cannot be calibrated in a universal fashion. This signal merely serves as proof that fluorescence occurs. The determination of the absolute cross section for molecular photoemission is therefore carried out indirectly as follows. We know that in the spectral range between 80.4 and 74.8 nm there are three decay channels available for the excited molecule, namely, ionization, dissociation into $\text{H} + \text{H}(n = 2)$, and fluorescence. Having calibrated two of these as discussed and knowing the absolute absorption cross section, we can get the third, the fluorescence cross section, by subtraction.

Figure 2 displays a section of the spectrum illustrating this procedure. Figures 2(a), 2(b), and 2(c) show the absorption, ionization, and dissociation cross sections, respectively, and Fig. 2(d) shows the molecular fluorescence cross section obtained by subtraction. Figure 2(e) displays the directly observed molecular emission which, as explained, is not on an absolute scale. Nevertheless, the comparison between Figs. 2(d) and 2(e) is gratifyingly good, showing that our data

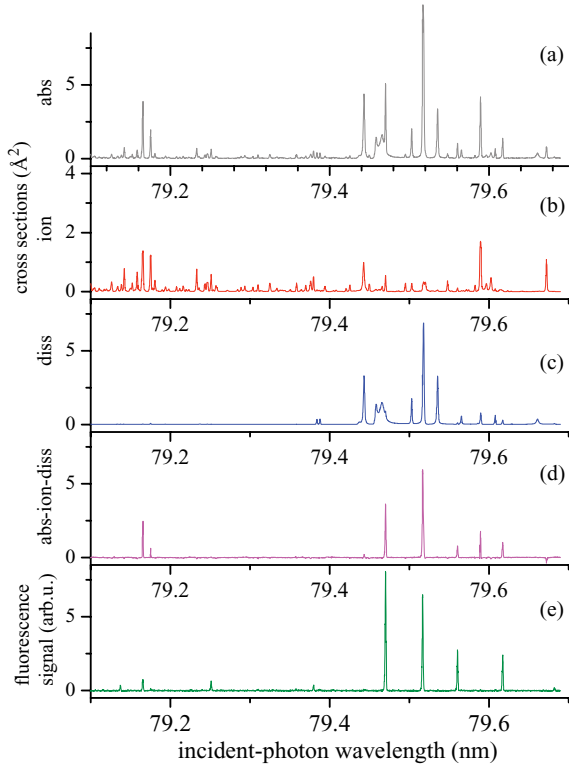


FIG. 2. (Color online) A section of the excitation spectra of H_2 above the ionization threshold. The spectra in (a)–(d) are on an absolute scale. (a) Photoabsorption, (b) photoionization, (c) photodissociation, (d) molecular fluorescence cross section obtained by subtraction, and (e) molecular fluorescence excitation spectrum recorded with a visible-sensitive detector.

are internally consistent and therefore that the cross-section calibrations are quantitatively meaningful. The comparison of Figs. 2(d) and 2(e) indicates further that the signal-to-noise ratio of the directly detected fluorescence signal is high, permitting the observation of weak emission lines that are not visible in Fig. 2(d).

III. THEORETICAL APPROACH

A. Clamped-nuclei quantum defects

The theoretical multichannel quantum defect approach used here has been discussed in numerous previous publications [17–19] and in particular in our preceding papers [5,12]. Briefly, we use quantum defect theory in its simplest form by disregarding channel interactions between singly excited and doubly (core) excited Rydberg channels. This means that we assume that the manifold of $^1\Pi_u$ excited states of H_2 represent a single unperturbed $np\pi$ Rydberg series converging to the $X^+2\Sigma_g^+$ ground state of H_2^+ . We have extracted the quantum defects from highly accurate theoretical clamped-nuclei (Born-Oppenheimer) potential energy curves [20,21]. Specifically, we have used the familiar one-channel Rydberg equation,

$$U_{np\pi}(R) = U^+(R) - \frac{1}{2[n - \mu_{np\pi}(R)]^2}, \quad (1)$$

written here in atomic energy units, in order to extract the quantum defects for $^1\Pi_u$ symmetry. $U_{np\pi}(R)$ is the

clamped-nuclei curve for the $np\pi$ Rydberg state, and $U^+(R)$ is the corresponding curve for the ion ground state, $X^+2\Sigma_g^+$. Note that the quantum defects determined in this way are functions of the internuclear distance R as well as of the energy because of the dependence on n appearing in Eq. (1). It is the R dependence that mediates the coupling between the electronic and the nuclear degrees of freedom. Details can be found in Ref. [12]. The set of clamped-nuclei quantum defect curves defined by Eq. (1) for different values of n is converted into an energy-dependent polynomial of the form

$$\begin{aligned} \mu(\epsilon, R) = & \mu^{(0)}(R) + [\epsilon(R)]\mu^{(1)}(R) \\ & + \frac{1}{2}[\epsilon(R)]^2\mu^{(2)}(R) + \frac{m}{M}\mu^{\text{specific}}(R), \quad (2) \end{aligned}$$

where $\epsilon(R) = U_{np\pi}(R) - U^+(R)$ is the binding energy of the Rydberg electron in the field of the core with the nuclei kept fixed at a distance R . The last term in Eq. (2) corresponds to the “specific” mass effect (mass polarization term) arising from the cross term $H'_3 = -(m/4M)\nabla_1\nabla_2$ in the molecular Hamiltonian (where m is the electron mass and M is the nuclear reduced mass). The required energy-normalized dipole transition moments are extracted from the available *ab initio* dipole transition moments from Refs. [20] and [21] in a fashion similar to what has just been described for the quantum defects.

B. Frame transformation

The frame transformation method has been implemented using well-documented MQDT technology [18,19,22]. In the case of the $Q(N)$ spectral lines and when hyperfine effects are neglected, the upper states are of pure $^1\Pi_u^-$ symmetry, and therefore there are no rotational channel couplings, with the result that only the vibrational frame transformation has to be applied. This is done by evaluating integrals of the type

$$\mu_{v^+N^+,v'^+N'^+}^{(q,N,d)} = \int \chi_{v^+N^+}(R)\mu^{(q)}(R)\chi_{v'^+N'^+}(R)dR, \quad (3)$$

where $N^+ = N'^+$ in the present case. $\mu^{(q)}$, with index $q = 0 - 2$, are the quantum defect functions of Eq. (2), and $\chi_{v^+N^+}(R)$ are the vibrational eigenfunctions of H_2^+ in the vibration-rotation level v^+, N^+ of the electronic ground state. The superscript N ($= N^+ = N'^+$ in the present situation) refers to the total angular momentum of the molecule exclusive of spins, while d refers to Kronig’s symmetry label designating levels that have total parity $-(-1)^N$.

The energy-dependent vibronic quantum defect matrix is expressed in terms of the vibrational integrals, Eq. (3), as

$$\begin{aligned} \mu_{v^+N^+,v'^+N'^+}^{(N,d)}(E) = & \mu_{v^+N^+,v'^+N'^+}^{(0,N,d)} + \bar{\epsilon}\mu_{v^+N^+,v'^+N'^+}^{(1,N,d)} \\ & + \frac{1}{2}\bar{\epsilon}^2\mu_{v^+N^+,v'^+N'^+}^{(2,N,d)}, \quad (4) \end{aligned}$$

where again $N^+ = N'^+ = N$ and where the reference energy $\bar{\epsilon}(E)$ is taken as the mean of the channel energies for each pair of coupled channels,

$$\bar{\epsilon} \equiv \bar{\epsilon}_{v^+N^+,v'^+N'^+}(E) = \frac{1}{2}[(E - E_{v^+N^+}^+) + (E - E_{v'^+N'^+}^+)]. \quad (5)$$

The mass-polarization term involving μ^{specific} in Eq. (2) is assumed to be included with $\mu_{v^+N^+,v'^+N'^+}^{(0,N,d)}$ (see Ref. [12]).

The vibronic quantum defect matrix $\mu_{v^+N^+,v''N''}^{(N,d)}(E)$ of Eq. (4) thus evaluated must, in the next step, be converted into vibronic matrices \mathcal{S} and \mathcal{C} , defined such that the vibronic reaction matrix \mathbf{K} is given by $\mathbf{K} = \mathcal{S}\mathcal{C}^{-1}$. These matrices are defined as $\mathcal{S} = \mathbf{U} \sin \pi \mu_\alpha \mathbf{U}^{\text{tr}}$ (with \sin replaced by \cos or \tan in the cases of \mathcal{C} and \mathbf{K} , respectively) [23], where \mathbf{U} is the eigenvector matrix of \mathbf{K} and μ_α are the associated eigenquantum defects. The conversion is carried out by employing the procedures described in Refs. [22] and [24].

C. Bound levels

The vibronic level energies are calculated using the well-known MQDT quantization condition

$$\sum_k [\cos(\pi v_j) \mathcal{S}_{jk} + \sin(\pi v_j) \mathcal{C}_{jk}] B_k = 0 \quad (6)$$

for each channel j . $v_j(E) = [-2(E - E_j^+)]^{-1/2}$ are the channel effective quantum numbers, and B_k are the channel mixing coefficients. The indices j and k run over all vibrational channels v^+N^+ specified above. Once an energy $E = E_n$ has been found such that Eq. (6) is satisfied for all j , the level energy, taken relative to the ionization potential and in wave number units, becomes

$$[(E_n - E_{v^+=0, N^+=0}^+)/hc] = -\frac{\mathcal{R}_{H_2}}{[v_{v^+=0, N^+=0}(E_n)]^2}, \quad (7)$$

where \mathcal{R}_{H_2} is the mass-corrected Rydberg constant and E_n is the level energy, in joules. Note that the use of the mass-corrected Rydberg constant instead of \mathcal{R}_∞ is equivalent to including the term $-(m/2M)\nabla_1^2$ of the molecular Hamiltonian, which, in the standard approach, is part of the adiabatic correction [23].

D. Discrete line intensities

An analogous procedure is applied to the clamped-nuclei transition dipole moments. These are used to calculate energy-dependent channel transition moments $d(\epsilon, R)$ with coefficients $d^{(q)}(R)$ analogous to the quantum defect coefficients $\mu^{(q)}$ of Eq. (2) (see Ref. [12] for details). Vibronic channel dipole transition matrix elements are then evaluated involving the vibrational wave function $\chi_{v''N''}(R)$ of the ground-state initial level. They have the form

$$d_{v^+N^+,v''N''}^{(q,N,d)} = \int \chi_{v^+N^+}(R) d^{(q)}(R) \chi_{v''N''}(R) dR, \quad (8)$$

where the superscript d (not to be confused with the dipole transition amplitude) refers to the upper-state Kronig symmetry and $\chi_{v''N''}(R)$ is the vibrational wave function in the ground-state initial level, which has Kronig symmetry c . We have $N = N'' = N^+$ here since we are dealing with Q transitions. The quantities $d_{v^+N^+,v''N''}^{(q,N,d)}$, $q = 0 - 2$, evaluated with the help of Eq. (8), are used to construct a set of energy-dependent vibronic transition moments in analogy with Eq. (4),

$$d_{v^+N^+,v''N''}^{(N,d)}(E) = d_{v^+N^+,v''N''}^{(0,N,d)} + \bar{\epsilon} d_{v^+N^+,v''N''}^{(1,N,d)} + \frac{1}{2} \bar{\epsilon}^2 d_{v^+N^+,v''N''}^{(2,N,d)}, \quad (9)$$

where the reference energy $\bar{\epsilon}(E)$ is taken as

$$\bar{\epsilon} \equiv \bar{\epsilon}_{v^+N^+}(E) = [(E - E_{v^+N^+}^+)]. \quad (10)$$

The effective transition moment to a bound Rydberg level n is given by the following superposition of channel amplitudes:

$$D_n = \frac{1}{\mathcal{N}} \sum_k d_{k,k''}(E_n) B_k(E_n), \quad (11)$$

where B_k are the channel mixing coefficients obtained by solving Eq. (6) and, again, k stands for the ionization channels v^+N^+ and k'' stands for $v''N''$. \mathcal{N} is the overall normalization factor of the bound-state wave function; see, e.g., Ref. [12] for detailed discussion and expressions. The transition moment D_n for each particular spectral line is finally converted into an upper-state emission probability by means of the relation

$$\begin{aligned} A_{n \rightarrow v''N''} &= \frac{4}{3} \frac{mc^2}{\hbar} \alpha^5 \left(\frac{E_n - E_{v''N''}}{2\mathcal{R}hc} \right)^3 \left| \frac{D_n}{a_0} \right|^2 \\ &= 2.142 \times 10^{10} \left(\frac{E_n - E_{v''N''}}{2\mathcal{R}hc} \right)^3 \left| \frac{D_n}{a_0} \right|^2 \text{ s}^{-1}. \end{aligned} \quad (12)$$

Here α is the fine-structure constant. The transition energy $E_n - E_{v''N''}$ is in joules, and the transition moment D_n is in meters. The ratios in the brackets (\dots) and $|\dots|$ correspond, respectively, to the transition energy and to the dipole transition moment, in atomic units.

E. Ionization continuum

Unlike in Ref. [12], we also account for the ionization channels that are open. The quantization condition for an open channel j reads [18]

$$\sum_k [\cos(\pi \tau_\rho) \mathcal{S}_{jk} - \sin(\pi \tau_\rho) \mathcal{C}_{jk}] B_k^{(\rho)} = 0, \quad (13)$$

where $\pi \tau_\rho$ is an open-channel ionization eigenphase and ρ is a solution index. Equation (13) replaces Eq. (6) for each line j of the linear algebraic system, Eq. (6), corresponding to an open channel. In total, there are as many eigenphases $\pi \tau_\rho$, $\rho = 1, \dots, N_P$ as there are open channels, and there is a set of channel mixing coefficients $B_k^{(\rho)}$ corresponding to each eigenphase $\pi \tau_\rho$.

The normalization of the continuum wave function is different from that applied to the bound levels. One defines open-channel amplitudes $T_{j,\rho}$ that form an $N_P \times N_P$ matrix \mathbf{T} . These matrix elements are given by [18]

$$\begin{aligned} T_{j,\rho} &= \sum_k \{ \cos[-\pi \tau_\rho(E)] \mathcal{C}_{j,k} - \sin[-\pi \tau_\rho(E)] \mathcal{S}_{j,k} \} B_k^{(\rho)}(E) \\ &\quad (k \in P + Q; j, \rho \in P), \end{aligned} \quad (14)$$

where Q denotes the N_Q closed channels and P denotes the N_P open channels. This expression resembles Eq. (13) except for a sign change and the fact that $\cos(-\pi \tau_\rho)$ and $\sin(-\pi \tau_\rho)$ have been interchanged. A further difference is that, in practice, at this stage the eigenphases $\pi \tau_\rho$ have already been determined along with the channel mixing coefficients $B_k^{(\rho)}$ (with the exception of an overall normalization factor for $B_k^{(\rho)}$). The matrix elements $T_{j,\rho}$ can thus be calculated for each column

ρ to within an overall factor. The matrix \mathbf{T} can be shown to be orthogonal (see, e.g., [18]). It becomes unitary if it is normalized according to

$$\sum_{j \in P} T_{j,\rho}^2 = 1 \quad (15)$$

for each ρ . This condition fixes the overall normalization of the N coefficients $B_k^{(\rho)}$ for each ρ by means of Eq. (14), and thus, it is the continuum analogue of the normalization factor \mathcal{N} appearing in Eq. (11). The matrix \mathbf{T} is known to coincide with eigenvector matrix of the open-channel (“physical”) electron-ion scattering matrix [18].

The total photoionization intensity that is of interest here is expressed in terms of a set of real dipole amplitudes, which replace Eq. (11):

$$D_\rho(E) = \sum_{k=1}^N d_{k,k'}(E) B_k^{(\rho)}(E). \quad (16)$$

The total ionization cross section is then proportional to

$$[D(E)]^2 = \sum_{\rho=1}^{N_p} [D_\rho(E)]^2. \quad (17)$$

The total photoionization cross section becomes, finally,

$$\sigma(E) = \frac{4}{3} \pi^2 \alpha (E - E_0) [D(E)]^2, \quad (18)$$

where, again, α denotes the fine-structure constant. Here D^2 has dimension $[E^{-1} L^2]$, so that $(E - E_0) D^2$ has dimension $[L^2]$. Therefore, if, for instance, the dipole operator implicit in Eq. (8) has been written in bohr units, the cross section will be in units of a_0^2 .

F. Dissociation continuum

The inclusion of dissociation channels into the MQDT framework has been described in previous papers [18,25,26]. Here we are concerned with very narrow line profiles so that the approach described in those papers may be simplified since we are able to neglect the interference between ionization and dissociation processes. We proceed as follows. Our treatment of dissociation is based on the realization that the dissociating state in the present problem is the $2p\pi C$ state and, as such, is simultaneously the lowest member of the $p\pi$ ionization channel (which we are considering here) and therefore plays a double role. This implies that the nonadiabatic coupling leading to vibrational autoionization of the $np\pi$ manifold above threshold is the same as that causing predissociation by the $2p\pi C$ state. Therefore, the vibronic quantum defect matrix elements $\mu_{v^+ N^+, v'^+ N^+}^{(N,d)}(E)$ of Eq. (4) contain all the information required to evaluate the predissociation widths in addition to the autoionization widths.

We exploit this circumstance by choosing specifically adapted vibrational basis sets for solving Eq. (6). This is illustrated by Fig. 3. Considering a specific value of the total energy E , we evaluate the vibrational wave functions χ_{v^+} and energies E_{v^+} by using a “large” vibrational basis, chosen such that it corresponds to electronically bound Rydberg channels only. This is achieved by omitting the channels with low v^+ , up to v_{lastopen}^+ , which would be open at the energy E (see

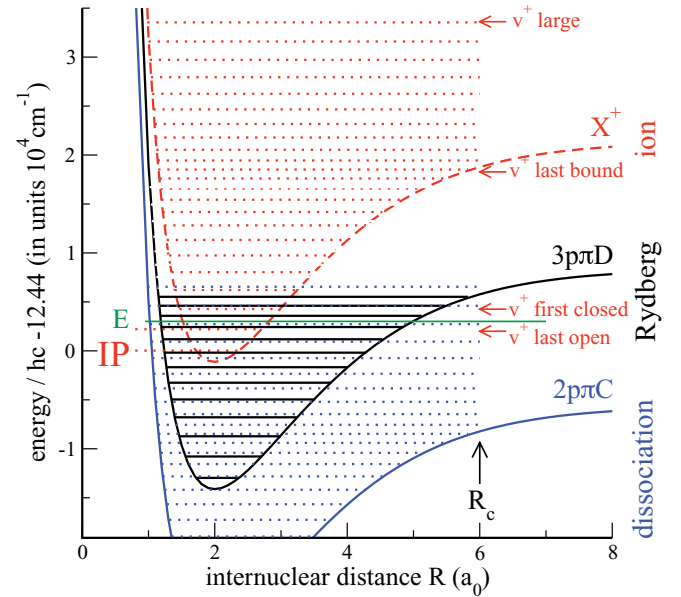


FIG. 3. (Color online) Molecular (solid lines) and ion (dashed line) potential energy curves with vibronic levels [black horizontal solid lines and dark gray (blue online) horizontal dotted lines] and vibrational ionization thresholds [light gray (red online) horizontal dotted lines], illustrating the discretization of the dissociation continuum through application of a fixed boundary condition at $R = R_c$. E [medium gray (green online) horizontal solid line] is the total energy under consideration. Rydberg levels with $n > 3$ are not shown, for clarity.

Fig. 3). The basis is taken as $v_{\text{firstclosed}}^+ \leq v^+ \leq v_{\text{large}}^+$, where $v_{\text{large}}^+ \approx 3 v_{\text{lastbound}}^+$ and where $v_{\text{lastbound}}^+$ corresponds to the last bound vibrational level of the ion core. The vibrational wave functions with $v^+ > v_{\text{lastbound}}^+$ reach out to $R = R_c$ (cf. Fig. 3). A common boundary condition $b = -\chi'/\chi$ is imposed on all $\chi_{v^+}(R)$ at $R = R_c$. With a large basis, the bound ion target vibrational levels ($v^+ < v_{\text{lastbound}}^+$) remain at their correct energies, but the level spectrum E_{v^+} now extends beyond the bound range into the H_2^+ vibrational continuum where the energies depend on the particular boundary condition b used. Similarly, solving Eq. (6) yields the Rydberg levels corresponding to $n \geq 3$ with $v < v_{\text{lastbound}}^+$ near their correct energies, but in addition, a set of fictitious Rydberg levels with $n = 2, v^+ > v_{\text{lastbound}}^+$ is obtained, which represents the discretized $2p\pi C$ state vibrational continuum, as illustrated in Fig. 3 (see also Ref. [25]).

When the boundary condition b at $R = R_c$ is varied, these levels may be tuned through the position of a bound Rydberg level with $n \geq 3, v^+ < v_{\text{lastbound}}^+$ (e.g., the level $3p\pi D, v = 9$ situated near E in Fig. 3). Vibronic interaction leads to an avoided crossing characterized by a closest approach $2V$. From this, the predissociation width Γ_d may be extracted using Fermi’s “golden rule”:

$$\Gamma_d = 2\pi \frac{V^2}{\Delta E}. \quad (19)$$

Here ΔE^{-1} is the density of levels with $n = 2, v^+ > v_{\text{lastbound}}^+$. An example of an avoided crossing permitting the determination of V is illustrated in Fig. 4 and concerns the

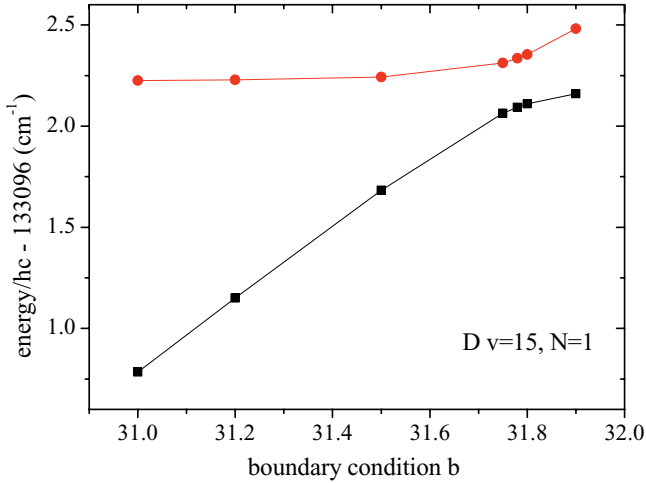


FIG. 4. (Color online) Level energies as functions of the boundary condition b applied to the vibrational wave functions at $R = R_c$. The anticrossing between a physical level ($D^1\Pi_u^-, v = 15, N = 1$ level, flat portions of the curves) and a fictitious continuum level ($C^1\Pi_u^-,$ steep portions of the curves) permits extraction of the predissociation width (see text for details).

$D^1\Pi_u^-, v = 15, N = 1$ level. ΔE , in turn, is evaluated by using the phase-amplitude Milne approach as implemented in Ref. [27]. This approach permits the evaluation of the phase $\phi(R_c)$ of the vibrational wave function, $\chi(R) \approx \alpha(R) \sin \phi(R)$, associated with the potential of the $2p\pi C$ dissociating state, accumulated between $R = 0$ and $R = R_c$. This may be done for arbitrary energy E , which is, in the present case, the energy at which the avoided crossing occurs. By calculating the accumulated phase for two energies separated by an infinitesimal increment, the rate of change of the accumulated phase may be obtained. The level density ΔE^{-1} is the inverse of this quantity.

G. Numerical details

The vibration-rotation wave functions $\chi_{v^+N^+}$ have been evaluated in the adiabatic approximation using the ion ground-state potential energy curve of Wind [28] and the adiabatic correction terms of Bishop and Wetmore [29]. The corresponding ion levels $E_{v^+N^+}^+$ are those of Wolniewicz and Orlikowski [30], evaluated including the nonadiabatic and relativistic interactions in addition to the adiabatic corrections. These ion level energies do not include the hyperfine interactions, but their accuracy is largely sufficient in the present context. We used the theoretical ionization potential $124\,417.491\text{ cm}^{-1}$ of Wolniewicz [31], which agrees with the most recent experimental value [32]. The vibronic matrices \mathcal{S} and \mathcal{C} were evaluated with variable basis sizes, as explained in Sec. III F, with $N^+ = 1, 2, 3,$ or 4 , whereby the vibrational wave functions were integrated from $R = 0.3$ out to R_c , with $R_c \approx 10\text{--}12$ a.u. or 25 a.u. in certain cases. Typical values are $v_{\text{firstclosed}}^+ = 0\text{--}3$, $v_{\text{lastbound}}^+ = 12$, and $v_{\text{large}}^+ = 50$. The ground-state vibrational wave function $\chi_{v''N''}(R)$ was evaluated with the potential energy curve of Wolniewicz [33].

IV. RESULTS

A. Observed spectra

We have observed 92 fluorescence lines originating from levels above the ionization threshold up the $H + H(n = 3)$ dissociation threshold (Tables I–III). Of these, 52 had been observed previously in 1977 and/or 1980 [34,35]. Eleven lines listed in these older publications have not been found in the present work. We suspect that these were artifacts arising from the background noise, which was larger in the earlier work. At the time, they were either left unassigned or attributed to high- n Rydberg levels. The large majority (67) of the present 92 fluorescence lines turns out to consist of $Q(N)$ transitions with N ranging from 1 to 4 (Table I), corresponding to upper levels of $^1\Pi_u^-$ symmetry. Eleven lines are R or P lines corresponding to excitation of $^1\Pi_u^+$ upper levels (Table II). A single fluorescence transition corresponds to $^1\Sigma_u^+$ upper-state symmetry ($7p\sigma, v = 2, N = 2$) (Table II). Among the 67 Q transitions giving rise to fluorescence, 32 belong to the $3p\pi D\text{-}X$ band system, 18 belong to the $4p\pi D'\text{-}X$ band system, and 14 belong to the $5p\pi D''\text{-}X$ band system. Only two lines are part of the corresponding Rydberg band system with $n = 6$, and a single transition belongs to $n = 7$. The R and P transitions are part of the $4p\pi D'\text{-}X$ and $5p\pi D''\text{-}X$ band systems. Thirteen fluorescence lines are as yet unassigned; they are listed in Table III. However, their presence is corroborated by the fact that they have also been observed in the photodissociation spectrum. We suspect that they might correspond to fluorescence from the $4f$ ($l = 3$) Rydberg complexes. These are, indeed, known [36] to give rise to an infrared emission spectrum, but the observations of Ref. [36] did not extend to the range above the ionization potential.

B. Line frequencies, intensities, and Franck-Condon factors

The frequencies and intensities of the $Q(N)$ transitions have already been discussed in a previous publication [12]. As discussed in Sec. II, the present measurements are significantly more precise and correspond to an uncertainty of about 1 cm^{-1} as compared to 6 cm^{-1} in our previous work. Simultaneously, the absolute intensity measurements have been improved. Figure 5 is a histogram summarizing the agreement between the present measurements of the 67 $Q(N)$ ($N = 1\text{--}4$) line frequencies and their calculation from first principles by MQDT. It may be seen that the present frequency measurements are beginning to approach the accuracy of the traditional spectrographic measurements, which are known to be better than a fraction of a wave number unit [13]. The histogram further confirms the fact that the *ab initio* MQDT calculations are globally correct to $\approx 1\text{ cm}^{-1}$. Figure 6 compares the measured and calculated Einstein A coefficients for most of the $Q(N)$ lines that give rise to fluorescence. Figure 7 is a histogram analogous to Fig. 5, which displays the observed to calculated ratios for the A coefficients. It is satisfying to see that this histogram peaks, indeed, very closely to 1, showing basic agreement between experiment and theory. The half-width of 17% is to be compared to the 10%–20% experimental relative uncertainty. It confirms the quality of the MQDT intensities. All these results are

TABLE I. $Q(N)$ transitions in ground-state absorption of H_2 giving rise to molecular fluorescence. ν/c is the observed transition energy, given in cm^{-1} . $E_{\text{obs}} - E_{\text{calc}}$ is the difference of observed and calculated level energies, given in cm^{-1} . A is the emission probability, given in 10^6 s^{-1} . γ_f , γ_d , and γ_i are fluorescence, dissociation, and ionization yields, respectively, given in %. Γ_f , Γ_d , and Γ_i are the fluorescence, dissociation, and ionization widths (full width at half maximum), respectively, given in cm^{-1} . Numbers in square brackets denote powers of 10.

State	ν	N	ν/c	$E_{\text{obs}} - E_{\text{calc}}$	A (obs)	A (calc)	γ_f (obs)	γ_d (obs)	γ_i (obs)	Γ_f (calc)	Γ_d (calc)	Γ_i (calc)	γ_f (calc)	γ_d (calc)	γ_i (calc)		
D	7	1	125 759.8	-0.6	24.0 ± 2.5	23.25	78 ± 3	24 ± 4	1.6 ± 0.2	1.70[-3]	2.1[-4]	5.53[-6]	89	11	0.3		
		2	125 601.1	-0.9	21.7 ± 2.3	22.20	77 ± 4	21 ± 2	1.0 ± 0.3	1.71[-3]	2.1[-4]	1.85[-6]	89	11	0.1		
		3	125 365.1	0.4	22.3 ± 1.3	20.91	80 ± 4	17 ± 2	1.5 ± 0.2	1.71[-3]	2.0[-4]	1.84[-8]	89	11	0.0		
		4	125 053.6	0.6	28 ± 4	24.15	65 ± 11	17 ± 2	16 ± 2	1.68[-3]	1.9[-4]	4.44[-4]	73	8.3	19.1		
		8	1	127 128.9	-0.9	13.5 ± 1.5	13.37	72 ± 3	27 ± 3	2.0 ± 0.3	1.68[-3]	2.6[-4]	2.26[-6]	87	13	0.1	
			2	126 964.2	-1.3	14.5 ± 1.5	13.32	80 ± 2	17 ± 2	2.0 ± 0.3	1.67[-3]	2.6[-4]	1.99[-5]	85	14	1.0	
			3	126 719.7	0.3	12.5 ± 1.1	13.25	81 ± 6	18 ± 2	2.3 ± 0.4	1.65[-3]	2.6[-4]	1.60[-5]	86	13	0.8	
			9	1	128 377.2	-0.6	8.3 ± 0.6	8.61	78 ± 9	21 ± 3	1.0 ± 0.2	1.69[-3]	2.7[-4]	2.59[-6]	86	14	0.1
			2	128 207.0	-0.8	8.6 ± 1.0	8.85	78 ± 5	22 ± 3	0.7 ± 0.3	1.70[-3]	2.6[-4]	4.18[-6]	86	13	0.2	
			3	127 953.6	0.5	8.2 ± 1.1	8.74	82 ± 5	19 ± 1	2.1 ± 1.2	1.70[-3]	2.6[-4]	2.21[-6]	87	13	0.1	
			10	1	129 501.9	-0.8	6.4 ± 0.8	5.84	76 ± 8	21 ± 3	1.7 ± 0.4	1.50[-3]	3.1[-4]	3.70[-6]	83	17	0.2
			2	129 325.8	-1.0	6.4 ± 0.7	5.80	75 ± 8	18 ± 2	5.2 ± 0.6	1.60[-3]	3.0[-4]	1.44[-5]	83	16	0.7	
			3	129 064.7	1.6	6.9 ± 1.3	5.20	68 ± 7	23 ± 3	8.7 ± 0.7	1.60[-3]	3.0[-4]	2.06[-4]	76	14	9.8	
			11	1	130 498.7	-0.9	4.9 ± 0.8	4.95	71 ± 9	24 ± 4	4.8 ± 0.8	1.64[-3]	3.1[-4]	8.51[-6]	84	16	0.4
			2	130 316.8	-0.7		5.01				1.66[-3]	2.9[-4]	2.65[-5]	84	14	1.3	
			3	130 045.4	0.7	6.1 ± 0.7	4.83	74 ± 11	22 ± 3	4.6 ± 4.6	1.64[-3]	2.8[-4]	1.05[-5]	85	15	0.5	
			12	1	131 364.6	-1.2	3.8 ± 0.4	3.14	76 ± 4	20 ± 2	3.5 ± 0.8	1.65[-3]	3.1[-4]	6.40[-5]	81	15	3.2
			2	131 175.8	-1.3	2.48 ± 0.3	3.06	67 ± 9	34 ± 6	4 ± 2	1.67[-3]	2.8[-4]	2.62[-5]	85	14	1.3	
			3	130 895.1	0.7		3.02				1.71[-3]	2.7[-4]	4.94[-5]	84	13	2.4	
			13	1	132 093.2	-0.5	1.8 ± 0.2	1.57	80 ± 8	20 ± 2	1.1 ± 0.7	1.63[-3]	2.7[-4]	4.37[-7]	86	14	0.0
			2	131 897.5	-0.5		1.40				1.62[-3]	2.7[-4]	1.06[-5]	85	14	0.6	
			3	131 606.4	0.3	0.6 ± 0.2	0.65				1.61[-3]	2.6[-4]	1.10[-5]	86	14	0.6	
			14	1	132 673.5	0.9	1.9 ± 0.2	1.58	67 ± 3	16 ± 2	18 ± 2	1.60[-3]	2.3[-4]	4.90[-4]	69	10	21.1
			2	132 470.3	-0.7	1.77 ± 0.2	1.36	70 ± 7	17 ± 2	18 ± 6	1.57[-3]	2.6[-4]	1.60[-4]	79	13	8.1	
			3	132 167.3	0.7	1.7 ± 0.5	1.31	84 ± 17	14 ± 5	3 ± 3	1.49[-3]	2.2[-4]	8.32[-5]	83	12	4.6	
			15	1	133 100.2	1.0	1.2 ± 0.1	0.95	84 ± 10	19 ± 2	1.4 ± 0.6	1.33[-3]	1.6[-4]	2.35[-5]	88	11	1.5
			2	132 888.8	-1.0	1.48 ± 0.2	0.82	68 ± 18	21 ± 3	3 ± 3	1.38[-3]	2.3[-4]	9.10[-6]	85	14	0.6	
			3	132 573.6	0.6		0.71				1.46[-3]	1.4[-4]	2.71[-6]	91	9.0	0.2	
			16	1	133 366.1	1.9	0.31 ± 0.04	0.35	95 ± 25	4 ± 4	4 ± 4	1.24[-3]	7.5[-5]	1.77[-6]	94	5.7	0.1
			2	133 145.1	-0.1		0.25				1.16[-3]	1.5[-4]	4.29[-6]	88	11	0.3	
			3	132 811.8	0.9	2.4 ± 0.3	2.09	78 ± 17	17 ± 7	6 ± 1	1.03[-3]	7.9[-5]	2.50[-5]	91	6.9	2.2	
			17	1	133 468.3	0.0	0.15 ± 0.04	0.09	89 ± 31	6 ± 6	6 ± 6	6.33[-4]	3.3[-5]	1.01[-9]	95	4.9	0.0
	D'	4	1	125 833.4	-0.8	15.1 ± 1.5	15.60	85 ± 2	6 ± 1	11 ± 1	7.68[-4]	1.8[-6]	1.02[-4]	88	0.2	12	
			2	125 690.6	-0.8	15.6 ± 1.0	16.33	80 ± 4	10 ± 1	11 ± 1	7.62[-4]	1.8[-6]	6.07[-5]	92	0.2	7	
			3	125 476.2	-1.8	21.6 ± 2.5	17.81	40 ± 5	5.1 ± 0.3	59 ± 4	7.48[-4]	1.8[-6]	1.42[-3]	35	0.1	65	
			4	125 197.1	-0.9		17.60				7.53[-4]	5.4[-5]	1.19[-4]	81	5.9	13	
			5	1	127 542.1	-1.3	16.9 ± 1.8	16.98	79 ± 3	7 ± 1	13 ± 2	7.15[-4]	3.9[-7]	8.67[-5]	89	0.0	11
				3	127 175.5	1.7	13.9 ± 2.0	19.18	11 ± 5	7 ± 4	91 ± 14	7.36[-4]	3.9[-7]	9.93[-3]	6.9	0.0	93
			6	1	129 139.6	-0.8	10.0 ± 1.1	12.20	28 ± 3	1 ± 1	71 ± 7	7.36[-4]	1.3[-6]	7.55[-3]	8.9	0.0	91
				2	128 986.4	-0.4	10.5 ± 0.7	12.12	11 ± 3	1.2 ± 0.4	89 ± 8	7.36[-4]	1.3[-6]	6.86[-3]	10	0.0	90
				3	128 758.4	1.5	10.1 ± 0.7	12.03	12 ± 2	1.8 ± 0.3	86 ± 8	7.35[-4]	1.3[-6]	6.11[-3]	11	0.0	89
				7	1	130 621.2	-1.1	6.2 ± 0.7	7.22	7 ± 5	0 ± 1	94 ± 10	7.36[-4]	2.6[-8]	1.62[-2]	4.3	0.0
			2	130 462.0	-1.2	7.2 ± 0.9	7.29	6 ± 6	2 ± 4	103 ± 12	7.34[-4]	2.6[-8]	1.45[-2]	4.8	0.0	95	
			3	130 225.4	0.5	7.4 ± 1.6	7.35	13 ± 10	20 ± 2	87 ± 17	7.33[-4]	2.6[-8]	1.29[-2]	5.4	0.0	95	
			8	1	131 986.4	-1.4	5.0 ± 0.3	5.41	13 ± 2	0 ± 1	89 ± 6	6.73[-4]	5.0[-6]	8.27[-3]	7.5	0.1	92
			2	131 822.4	-0.9	5.6 ± 0.9	5.29	55 ± 3	0.4 ± 0.7	41 ± 3	7.21[-4]	5.0[-6]	5.33[-4]	57	0.4	42	
			3	131 576.4	0.6	4.9 ± 0.5	5.87	74 ± 6	11 ± 1	21 ± 4	7.29[-4]	5.0[-6]	4.08[-4]	64	0.4	36	
			9	1	133 238.4	-1.8	3.1 ± 0.4	3.16	26 ± 5	3 ± 0	71 ± 8	7.05[-4]	1.9[-6]	2.56[-3]	22	0.1	78
			2	133 068.7	-1.4	3.1 ± 0.4	3.20	21 ± 7	3.2 ± 0.6	75 ± 8	7.03[-4]	1.9[-6]	2.05[-3]	26	0.1	74	
			3	132 819.2	0.7	1.3 ± 0.3	1.08	65 ± 17	8 ± 2	25 ± 3	5.06[-4]	1.9[-6]	3.59[-4]	58	0.2	41	
D''	2	1	124 382.3	-0.8	4.0 ± 0.2	4.02	1.9 ± 1.7	1.0 ± 1.7	97 ± 2	3.31[-4]	3.4[-9]	1.27[-2]	2.5	0.0	97		
		3	1	126 317.9	-1.3	13.2 ± 1.6	12.37	53 ± 3	0.8 ± 0.1	46 ± 4	3.35[-4]	2.2[-7]	6.59[-3]	4.8	0.0	95	
			2	126 181.2	-1.0	12.5 ± 1.4	12.93	21 ± 4	2.8 ± 0.3	76 ± 8	3.88[-4]	2.8[-7]	1.91[-3]	17	0.0	83	
			3	125 976.7	-0.4	11.9 ± 1.3	13.09	12 ± 4	2.0 ± 0.3	89 ± 9	3.88[-4]	3.0[-7]	2.68[-3]	13	0.0	87	
			4	1	128 141.8	-2.7	8.3 ± 0.9	9.94	22 ± 2	2.9 ± 0.4	79 ± 8	3.85[-4]	1.6[-7]	4.84[-3]	7.4	0.0	93
			2	127 999.9	-1.9	9.0 ± 1.0	9.23	22 ± 4	2.6 ± 0.3	76 ± 9	3.76[-4]	1.6[-7]	1.89[-3]	17	0.0	83	
			3	127 787.1	-0.6	7.3 ± 0.9	10.72	6 ± 5	0.3 ± 0.1	94 ± 11	3.77[-4]	1.4[-7]	1.36[-2]	2.7	0.0	97	
			5	1	129 853.2	1.5	5.7 ± 0.6	7.40	12 ± 5	0.4 ± 0.1	88 ± 10	3.81[-4]	1.4[-8]	1.42[-2]	2.6	0.0	97
			2	129 700.9	-2.4	7.5 ± 1.2	7.29	8 ± 5	0.1 ± 0.1	91 ± 14	3.81[-4]	1.9[-8]	1.24[-2]	3.0	0.0	97	
			3	129 480.3	-1.1	6.2 ± 0.7	7.06	9 ± 5	0.3 ± 0.1	92 ± 10	3.79[-4]	3.1[-8]	9.18[-3]	4.0	0.0	96	

TABLE I. (*Continued.*)

State	v	N	ν/c	$E_{\text{obs}} - E_{\text{calc}}$	A (obs)	A (calc)	γ_f (obs)	γ_d (obs)	γ_i (obs)	Γ_f (calc)	Γ_d (calc)	Γ_i (calc)	γ_f (calc)	γ_d (calc)	γ_i (calc)
	6	1	131 443.1	0.0	4.7 ± 0.5	5.57	11 ± 7	0.6 ± 0.6	92 ± 10	3.76[-4]	8.7[-9]	4.40[-2]	0.8	0.0	99
		2	131 285.6	-3.7		5.51				3.77[-4]	4.4[-8]	0.03792	1.0	0.0	99
		3	131 058.2	-1.0		5.43				3.77[-4]	8.3[-8]	3.28[-2]	1.1	0.0	99
	7	1	132 920.8	0.3	6.8 ± 0.7	3.95	10 ± 9	1.2 ± 0.2	89 ± 9	3.77[-4]	2.0[-7]	5.25[-2]	0.7	0.0	99
	$6p\pi$	2	125 645.1	-0.7	10.4 ± 1.1	11.28	49 ± 7	19 ± 2	40 ± 5	1.82[-4]	1.1(-10)	6.74[-2]	0.3	0.0	100
	3	1	127 593.7	0.5	2.5 ± 0.3	3.65	11 ± 5	1 ± 1	91 ± 11	2.45[-4]	1.3[-9]	3.49[-2]	0.7	0.0	99
$7p\pi$	3	1	128 366.6	1.1	3.2 ± 0.4	3.64	1 ± 5	0 ± 0	98 ± 12	1.34[-4]	2.5[-8]	2.02[-2]	0.7	0.0	99

collected in Table I. The theoretical evaluation of the Einstein A coefficients has been carried out not only for the transitions with $v'' = 0$ but also for all bound levels ($v'' > 0$). This enables the upper-state lifetimes and the relative band strengths $f_{v',v''=0} = A_{v',v''=0} / \sum_{v''} A_{v',v''}$ to be calculated.

C. General discussion of partial yields

We determined the yields γ_f , γ_d , and γ_i , which correspond to photoinduced fluorescence, photodissociation, and photoionization, respectively, on the basis of the absolute line intensities measured in absorption I_{abs} and in the three different decay channels, I_f , I_d , and I_i , according to

$$\gamma_f = I_f / I_{\text{abs}}, \quad (20)$$

with similar expressions for γ_d and γ_i . Figure 8 displays the photoionization, photodissociation, and fluorescence yields for the $3p\pi D$, $4p\pi D'$, and $5p\pi D''^1\Pi_u^-$ levels with $N = 1, 2$, and 3 along with the previously measured values [4,37]. Note that the present measurements are more precise and complete. We see that fluorescence dominates for $n = 3$ (D state) and is still present for $n = 4$ and 5 (D' and D'' states). Photodissociation is significant ($\approx 15\%$ – 20%) for $n = 3$ but is absent for $n = 4$ and 5. Photoionization is dominant for $n = 5$. For $n = 4$, it varies substantially as function of the vibrational quantum number and of the rotational quantum number N , whereas for $n = 3$, ionization is a minor channel. Note, in any case, that the global trends do not significantly depend on the rotational quantum number.

By using the partial widths calculated for ionization, Γ_i , for dissociation, Γ_d , and for fluorescence, Γ_f , which will be discussed in more detail in the following Secs. IV D, IV E, and IV F we can evaluate the corresponding theoretical yields γ from expressions of the type, for instance,

$$\gamma_f = \frac{\Gamma_f}{\Gamma_i + \Gamma_d + \Gamma_f}. \quad (21)$$

The values obtained in this way are displayed in Fig. 8 as well as in Table I. The agreement between experiment and theory is remarkable considering the variety of different situations that occur.

D. Fluorescence yields and widths

The natural widths corresponding to fluorescence have been determined from the experiment by dividing the measured A coefficients for absorption from $v'' = 0$ by the corresponding relative band strengths. The band strengths have been obtained from the calculations (cf. Sec. IV B), and in that sense, the natural fluorescence widths obtained here are not purely experimental. The experimental ionization and dissociation widths, in turn, are obtained from the fluorescence widths combined with the various experimental yields. These values are displayed in Figures 9, 10, and 11.

With regard to the $6p\pi Q(1)$ transitions ($v = 2 - 6$), we can say the following: these transitions are clearly seen in the fluorescence excitation cross section obtained by subtraction, whereas only the lines corresponding to $v = 2$ and 3 are directly observed in the molecular fluorescence signal. This

TABLE II. $R(0)$, $R(1)$, $R(2)$, and $P(2)$ transitions in ground-state absorption of H_2 giving rise to molecular fluorescence. ν/c is the transition energy, in cm^{-1} . A is the emission probability, in 10^6 s^{-1} . γ_f , γ_d , and γ_i are fluorescence, dissociation, and ionization yields, respectively, given in %.

State	v	Transition	$\nu/c(\text{obs})$	$A(\text{obs})$	$\gamma_f(\text{obs})$	$\gamma_d(\text{obs})$	$\gamma_i(\text{obs})$
$4p\pi D'$	5	$R(0)$	127 666.3	6.7 ± 0.9	8 ± 6	6 ± 1	86 ± 10
		$R(1)$	127 639.4	6.3 ± 0.6	13 ± 4	71 ± 7	15 ± 2
	6	$R(1)$	129 198.6	8.5 ± 0.9	14 ± 5	78 ± 8	8 ± 1
	9	$R(0)$	133 357.0	3.2 ± 0.3	2 ± 6	46 ± 5	61 ± 7
$5p\pi D''$		$R(1)$	133 301.4	2.9 ± 0.3	3 ± 7	74 ± 8	24 ± 3
	2	$R(1)$	124 493.7	5.2 ± 0.5	24 ± 4	4.5 ± 0.5	71 ± 7
		$R(2)$	124 422.0	3.8 ± 0.4	11 ± 5	10 ± 1	82 ± 9
	3	$R(0)$	126 442.2	5.4 ± 0.4	12 ± 5	2.1 ± 0.4	86 ± 14
		$R(1)$	126 426.4	3.4 ± 0.4	20 ± 6	12 ± 1	73 ± 8
		$P(2)$	126 087.4	19.1 ± 3.4	3 ± 9	2.6 ± 0.4	93 ± 12
	5	$R(1)$	129 924.5	6.2 ± 0.7	12 ± 4	5 ± 1	72 ± 8
$7p\sigma$	2	$R(1)$	126 302.5	9.5 ± 1.1	33 ± 6	3.7 ± 0.4	66 ± 8

TABLE III. Unassigned transitions in ground-state absorption of H_2 giving rise to molecular fluorescence. ν/c is the transition energy, in cm^{-1} . γ_f , γ_d , and γ_i are fluorescence, dissociation, and ionization yields, respectively, given in %.

$\nu/c(\text{obs})$	$\gamma_f(\text{obs})$	$\gamma_d(\text{obs})$	$\gamma_i(\text{obs})$
125 499.0	26 ± 30	82 ± 9	4 ± 1
126 362.6	17 ± 11	39 ± 5	33 ± 21
127 320.6			
127 692.7			
128 160.9	1 ± 6	10 ± 2	89 ± 13
129 834.9	10 ± 5	2.3 ± 0.4	83 ± 16
129 921.7	20 ± 5	26 ± 5	64 ± 11
130 294.9			
131 170.4	20 ± 5	9 ± 1	72 ± 8
131 590.9			
132 483.7			
132 591.5			
133 168.1			

may be due to an insufficient sensitivity of the visible fluorescence detection related to the spectral range where the higher ν levels emit. We note, nevertheless, that the corresponding fluorescence yields are calculated to amount to less than 1%.

The autoionization width of the $7p\pi, \nu = 3 Q(1)$ line is calculated to be $2 \times 10^{-2} \text{ cm}^{-1}$, which implies a fluorescence yield of 0.7%, in agreement with the observed value $1\% \pm 1\%$. Together with the $7p\sigma, \nu = 2 R(1)$ line, to be discussed in Sec. IV G, this value is the highest principal quantum number for which molecular fluorescence has been observed so far.

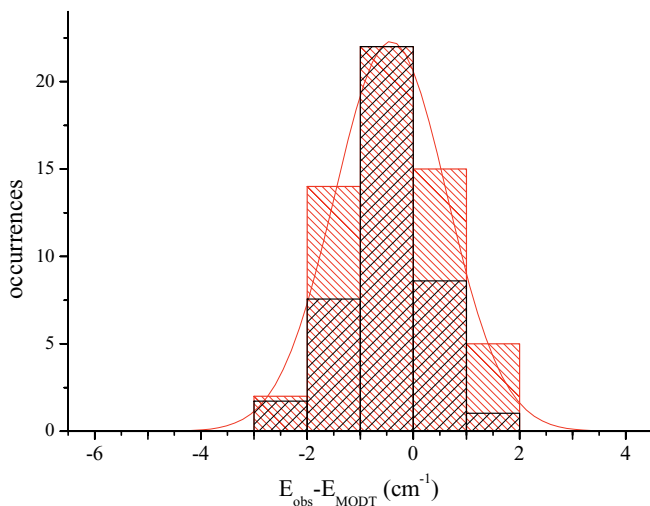


FIG. 5. (Color online) Histogram illustrating the overall comparison between measured and calculated $Q(N)$ absorption line positions. Hatched (red online) bars show the present measurements. The curve is the Gaussian that fits the histogram. Black cross-hatched bars show spectrographic measurements [13–15] normalized to fit the maximum of the curve.

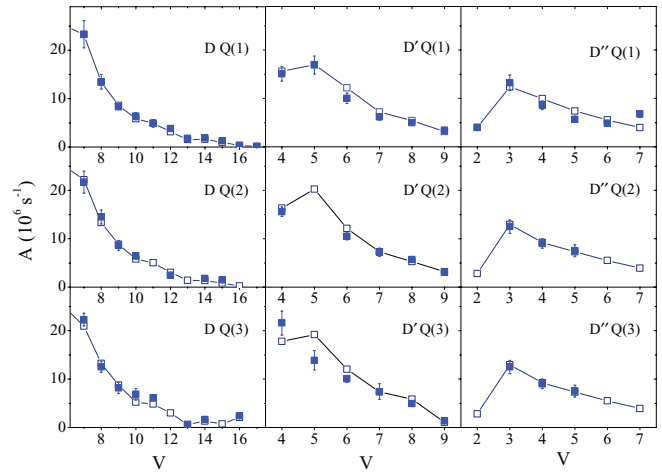


FIG. 6. (Color online) Measured (solid squares, in blue online) and calculated (open squares connected by lines) Einstein A coefficients for the $3p\pi D$, $4p\pi D'$, and $5p\pi D'' \ ^1\Pi_u^-, N = 1 - 3$ levels, plotted as functions of the vibrational quantum number ν .

E. Photoionization cross sections, yields, and widths

Figure 12 represents the photoionization spectrum, calculated by neglecting the other two decay channels. Strictly speaking, this spectrum represents the theoretical photoabsorption spectrum, broadened by interaction with the open ionization continua, but unaffected by the dissociation and fluorescence processes. A logarithmic intensity scale has been used in Fig. 12 in order to show all the resonances. Interestingly, a relatively small number of lines is seen to exceed the background formed by the rather regular high- n Rydberg structures by four to six orders of magnitude. With the overall intensity distribution being relatively smooth, this means that these strong ionization peaks correspond to exceedingly small widths (see below). It turns out that these are precisely the transitions to upper levels that are long-lived enough to be able to fluoresce. Note, incidentally, that the apparent profile asymmetry of the resonances seen in Fig. 12 is drastically enhanced by the logarithmic ordinate scale.

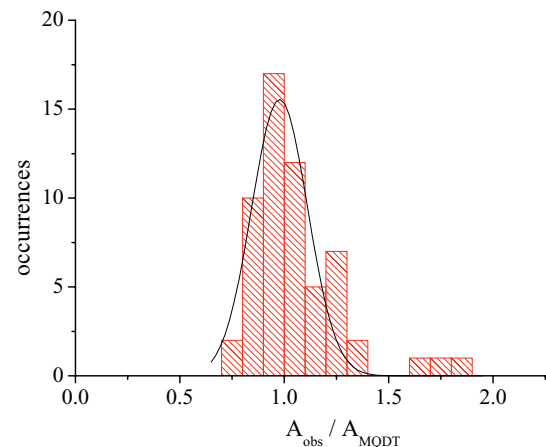


FIG. 7. (Color online) Histogram illustrating the overall comparison between measured and calculated absorption line intensities (Einstein A coefficients). The three outliers probably correspond to blended lines. The curve is the Gaussian that fits the histogram.

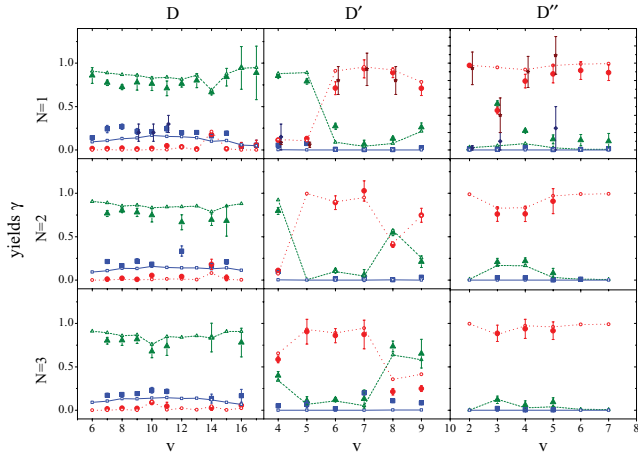


FIG. 8. (Color online) Comparison between measured and calculated yield values for the $3p\pi D$, $4p\pi D'$, and $5p\pi D''$ $^1\Pi_u^-$ levels, plotted as functions of the excited-state vibrational quantum number v . Triangles (green online, dashed lines) refer to fluorescence, squares (blue online, solid lines) refer to dissociation, and circles (red online, dotted lines) refer to ionization, respectively. Open symbols connected by lines are calculated values, whereas solid symbols are measured values. Previously measured values [4,37] are also indicated and, for better visibility, slightly offset to the right on the abscissa scale.

Figure 13 compares the experimental fluorescence excitation spectrum (upper graph) with the calculated ionization spectrum from Fig. 12 plotted on a linear intensity scale. The similarity between the two spectra is, indeed, striking. This result may seem surprising at first glance, but it is readily understood when one considers the relationship between the cross-section profile maximum σ_{\max} and the integrated line intensity I_{disc} . For a Lorentzian line shape this reads

$$\sigma_{\max} = \frac{2}{\pi\Gamma} I_{\text{disc}}, \quad (22)$$

showing that very narrow (i.e., long-lived) resonances are strongly enhanced in the unconvoluted theoretical spectrum. The theoretical photoionization spectrum has been used to determine the partial ionization widths of the excited levels included in Table I. We turn now to their detailed discussion.

As already stated, the calculated ionization widths of the fluorescing $3p\pi D$ $^1\Pi_u^-$, v levels are very small; they lie in the range 10^{-7} to 10^{-5} cm^{-1} . This arises because autoionization can occur only through vibrational interaction with $\Delta v = 7$ or larger. The fluctuations of the widths are due to very weak local perturbations with higher Rydberg levels which autoionize more rapidly. Autoionization of the $4p\pi D'$ $^1\Pi_u^-$ vibrational levels is possible via $\Delta v \geq 3$ processes and is therefore expected to be more rapid. The corresponding autoionization widths are, indeed, found to be about two orders of magnitude larger as compared to the $3p\pi D$ state levels. The local perturbations are also stronger. For example, the $4p\pi D'$, $v = 5$, $N = 2$ level is mixed with $10p\pi$, $v = 2$, $N = 2$. This latter level is strongly autoionized, with a corresponding partial width of the order of 0.1 cm^{-1} . The effective width of the perturbed $4p\pi D'$ level is then too large to allow the fluorescence to be detected, as is, indeed, experimentally confirmed. Autoionization of the $5p\pi D''$ vibrational levels

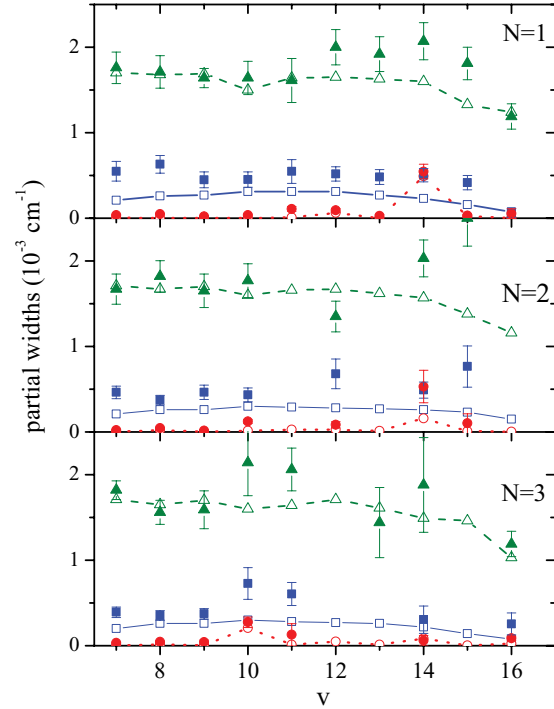


FIG. 9. (Color online) Measured and calculated partial widths for the $3p\pi D$ $^1\Pi_u^-$ levels plotted as functions of v . The symbols have the same meanings as in Fig. 8.

can occur with $\Delta v \geq 2$. The autoionization widths calculated for these levels are of the order of 10^{-2} cm^{-1} , with the result that ionization is now the dominant decay channel.

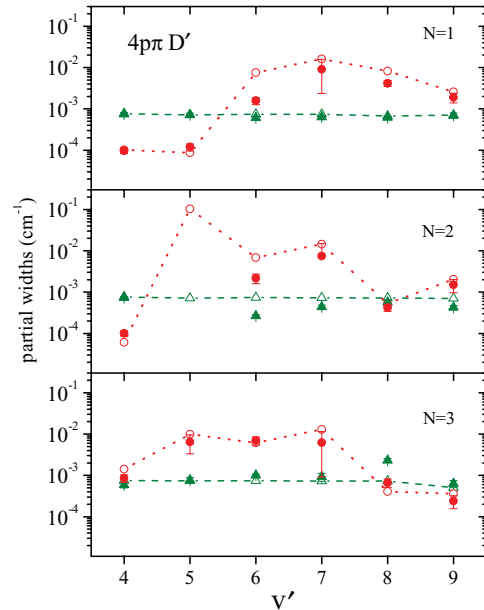


FIG. 10. (Color online) Measured and calculated partial widths for the $4p\pi D'$ $^1\Pi_u^-$ levels plotted as functions of v . The symbols have the same meanings as in Fig. 8. Note the logarithmic ordinate scale.

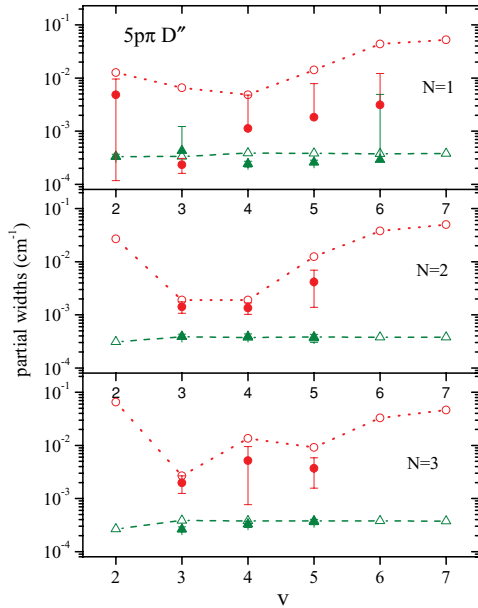


FIG. 11. (Color online) Measured and calculated partial widths for the $5p\pi D'' \ ^1\Pi_u^-$ levels plotted as functions of v . The symbols have the same meanings as in Fig. 8. Note the logarithmic ordinate scale.

F. Predissociation yields and widths

The dissociation widths of the $^1\Pi_u^-$ levels have been evaluated theoretically, as described in Sec. III F, for the vibrational levels of the $3p\pi D$, $4p\pi D'$, and $5p\pi D''$ states. They were found to range between 4×10^{-4} and $1 \times 10^{-3} \text{ cm}^{-1}$ for the D state, and they are calculated to be at least two orders of magnitude smaller for the D' and D'' states. The calculations thus reproduce the experimental observation that dissociation is negligible for the D' and D'' states. Recall that the dissociation involves the $2p\pi C \ ^1\Pi_u^-$ continuum. The vibronic coupling between $n = 2$, on the one hand, and $n' = 3, 4$, and 5 , on the other hand, decreases rapidly with n' , as had already been noted by Wolniewicz [38]. The comparison

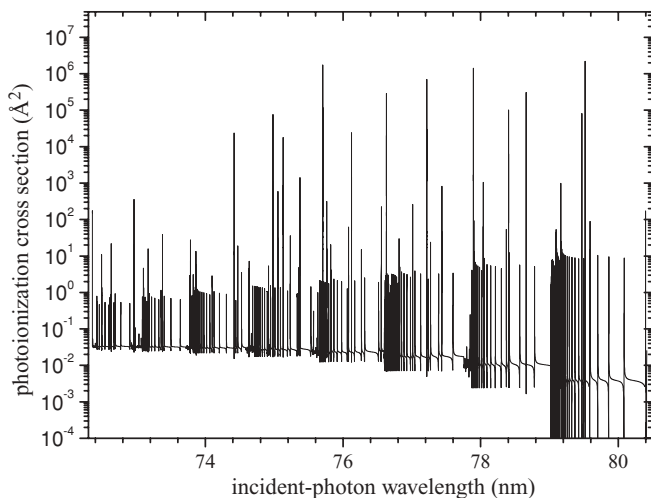


FIG. 12. Photoionization cross section calculated for $Q(1)$ transitions plotted on a logarithmic scale. The dissociation and fluorescence decay channels have not been taken into account in this calculation.

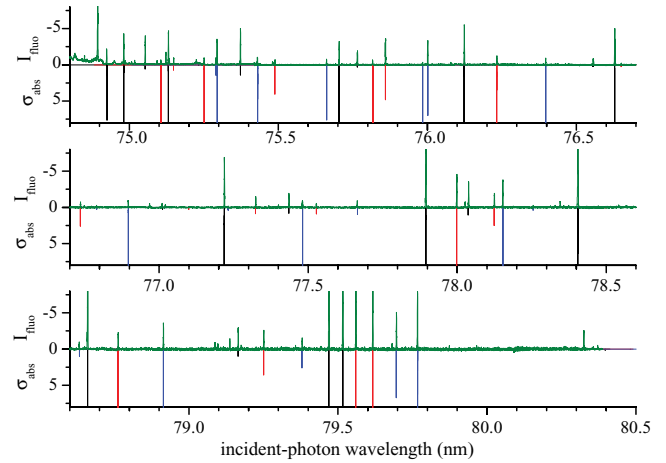


FIG. 13. (Color online) Upper traces (green online): experimental fluorescence excited spectrum plotted on a linear scale (arbitrary units). Lower traces: theoretical photoionization cross sections calculated for the $Q(1)$, $Q(2)$, and $Q(3)$ transitions [in black, light gray (red), and dark gray (blue), respectively] plotted on a linear scale (in units of 10^{-13} cm^2).

between measured and calculated widths (see, in particular, Figs. 10 and 11) is seen to be quite good despite the fact that the various decay widths vary by many orders of magnitude. The yields resulting from the calculations of the various partial widths are included in Fig. 8 where they are compared with the experimental values.

G. Competition between decay processes in $R(0)$, $R(1)$, and $P(2)$ transitions

As stated in Sec. IV A, molecular fluorescence competing with dissociation and ionization has been observed for 12 $R(0)$, $R(1)$, and $P(2)$ lines. The experimental results are listed in Table II. Their systematic study by theory is deferred to a future presentation, but, in fact, some values already exist in the literature [25,39]. In particular, the $4p\pi D' \ ^1\Pi_u^+$, $v = 5, N = 1$ and 2 levels have been treated theoretically [39]. We excite these levels through the $R(0)$ and $R(1)$ transitions, and we have observed fluorescence. We have thus determined the fluorescence, dissociation, and ionization yields, but since in the theoretical calculation of Ref. [39] fluorescence has not been included, we limit our discussion here to the ionization and dissociation processes. Our measured value for the yield $\Gamma_i/(\Gamma_i + \Gamma_d)$, viz., $17.6\% \pm 0.7\%$ for excitation via the $R(1)$ line, compares very well with the calculation (17%). The same is true for excitation via the $R(0)$ line ($93.7\% \pm 1.2\%$ versus 93%). However, the calculated widths are too large by a factor of about 3 or 4 in order to allow for the fluorescence, which is observed to contribute 13% to the total yield in the $R(1)$ line and 8% in the $R(0)$ line. This discrepancy remains unexplained at this stage.

The $R(0)$ and $R(1)$ transitions corresponding to excitation of $5p\pi D'' \ ^1\Pi_u^+$, $v = 2, N = 1$ and 2 from $X \ ^1\Sigma_g^+$, $v = 0, N = 0$ and 1, respectively, are not resolved in our absorption spectrum. However, their dynamics can be evaluated separately owing to the fact that only the upper level of the $R(1)$

line fluoresces. The corresponding $R(2)$ line is also seen in fluorescence, as are the $R(1)$ lines corresponding to $v = 3$ and 5. The fluorescence yield for the $R(1)$ transition leading to $7p\sigma, v = 2, N = 2$ is astonishingly high; it has been measured to correspond to $33\% \pm 7\%$. This is the only excited level of H_2 situated above the ionization potential of predominant $^1\Sigma_u^+$ symmetry, which is known to fluoresce [35].

Owing to its intrinsic weakness, predissociation of the upper levels of the $Q(N)$ transitions belonging the $4p\pi D'-X$ and $5p\pi D''-X$ band systems is difficult to measure. This is not the case for the corresponding $R(N)$ transitions whose dissociation yields amount to about 70%–80% in the $4p\pi D'-X$ band system and to 5%–15% in the $5p\pi D''-X$ band system, respectively. The upper states of these latter examples have c Kronig symmetry and hence correspond to multichannel situations with a larger number of channels involved and increased possibilities for local perturbations between quasibound levels. For example, the $4p\pi^-$ manifold (d Kronig symmetry) can directly predissociate only to the $2p\pi^-C$ dissociation continuum, whereas for the $4p\pi^+$ manifold the $3p\sigma^+B'$ dissociation continuum is also available and actually largely dominates. The indirect process involves the interfering channels $3p\pi^+$ or $4p\sigma^+$ [40]. Identical mechanisms are active in the predissociation of the $5p\pi^+$ manifold but are less efficient because of the larger change of the principal quantum number n (i.e., larger electronic energy gap) required by the process.

V. CONCLUSION

In this paper we have presented detailed evidence for slow decay processes active in numerous superexcited molecular levels of H_2 . These processes take place typically on the sub- μ s scale but are slower than 1 ns. Due to our absolute absorption and partial decay cross-section measurements, we have been

in a position to characterize these slow processes in detail, despite the fact that the corresponding natural widths of the excited states studied here are orders of magnitude smaller than our experimental spectral resolution. The theoretical approach implemented in this work fully accounts for the observed dynamics and includes autoionization, predissociation, and spontaneous photon emission. While our theoretical approach as such is not new and has been shown previously to be a powerful tool for the description of many aspects of the internal dynamics of molecular hydrogen (see, e.g., various papers collected in Ref. [19]), it has been applied here in an unprecedented systematic way. It appears that MQDT is capable of describing the various very weak couplings quite accurately, involving both vibronic interaction and radiative decay.

The observation and characterization of spontaneous photon emission in a large number of superexcited levels constitutes a remarkable exception in the field of molecular physics in general. It will be interesting to explore the question of to what extent the slow dynamics studied in the present work may have implications for the physics of the interstellar medium and of planetary atmospheres.

ACKNOWLEDGMENTS

We acknowledge the Helmholtz-Zentrum Berlin electron storage ring BESSY II for provision of synchrotron radiation at beam line U125/2-10m-NIM. The research leading to these results has received funding from the European Community's Seventh Framework Programme (FP7/2007-2013) under Grant No. 226716. Ch.J. thanks the Miescher Foundation (Basel, Switzerland) for partial support. Ch.J. was further supported by the ANR (France) under Contract 09-BLAN-020901. He is grateful to Dr. A. Kirrander (Orsay) for helpful suggestions concerning the manuscript.

-
- [1] W. A. Pryor *et al.*, *J. Geophys. Res.* **103**(E9), 20149 (1998).
 [2] K. Gillmon, J. M. Shull, J. Tumlinson, and C. Danforth, *Astrophys. J.* **636**, 891 (2006).
 [3] W. Sroka, *Phys. Lett. A* **28**, 784 (1969).
 [4] P. M. Guyon, J. Breton, and M. Glass-Maujean, *Chem. Phys. Lett.* **68**, 314 (1979).
 [5] M. Glass-Maujean, Ch. Jungen, H. Schmoranzner, A. Knie, I. Haar, R. Hentges, W. Kielich, K. Jänkälä, and A. Ehresmann, *Phys. Rev. Lett.* **104**, 183002 (2010).
 [6] M. Glass-Maujean, S. Klumpp, L. Werner, A. Ehresmann, and H. Schmoranzner, *J. Phys. B* **40**, F19 (2007).
 [7] M. Glass-Maujean, S. Klumpp, L. Werner, A. Ehresmann, and H. Schmoranzner, *Mol. Phys.* **105**, 1535 (2007).
 [8] M. Glass-Maujean, S. Klumpp, L. Werner, A. Ehresmann, and H. Schmoranzner, *J. Chem. Phys.* **126**, 144303 (2007).
 [9] M. Glass-Maujean, S. Klumpp, L. Werner, A. Ehresmann, and H. Schmoranzner, *J. Mol. Spectrosc.* **249**, 51 (2008).
 [10] G. Reichardt *et al.*, *Nucl. Instrum. Methods Phys. Res., Sect. A* **467-468**, 462 (2001).
 [11] R. Follath and A. Balzer, *AIP Conf. Proc.* **1234**, 657 (2010).
 [12] M. Glass-Maujean and Ch. Jungen, *J. Phys. Chem. A* **113**, 13124 (2009).
 [13] G. Herzberg and Ch. Jungen, *J. Mol. Spectrosc.* **41**, 425 (1972).
 [14] S. Takezawa, *J. Chem. Phys.* **52**, 2575 (1970).
 [15] H. Abgrall, E. Roueff, F. Launay, and J. Y. Roncin, *Can. J. Phys.* **72**, 856 (1994).
 [16] G. D. Dickenson *et al.*, *J. Chem. Phys.* **133**, 144317 (2010).
 [17] M. J. Seaton, *J. Phys. B* **46**, 167 (1983) (reprinted in Ref. [19]).
 [18] C. H. Greene and Ch. Jungen, *Adv. At. Mol. Phys.* **21**, 51 (1985).
 [19] *Molecular Applications of Quantum Defect Theory*, edited by Ch. Jungen (Institute of Physics, Bristol, 1996).
 [20] L. Wolniewicz and G. Staszewska, *J. Mol. Spectrosc.* **220**, 45 (2003).
 [21] [<http://www.fizyka.umk.pl/ftp/publications/ifiz/luwo/>].
 [22] S. C. Ross and Ch. Jungen, *Phys. Rev. A* **49**, 4364 (1994) (reprinted in Ref. [19]).
 [23] Ch. Jungen and O. Atabek, *J. Chem. Phys.* **66**, 5584 (1977) (reprinted in Ref. [19]).
 [24] N. Y. Du and C. H. Greene, *J. Chem. Phys.* **85**, 5430 (1986).
 [25] H. Gao, Ch. Jungen, and C. H. Greene, *Phys. Rev. A* **47**, 4877 (1993).
 [26] A. Matzkin, Ch. Jungen, and S. C. Ross, *Phys. Rev. A* **62**, 062511 (2000).

- [27] Ch. Jungen and F. Texier, *J. Phys. B* **33**, 2495 (2000).
- [28] H. Wind, *J. Chem. Phys.* **42**, 2371 (1965).
- [29] D. M. Bishop and R. W. Wetmore, *Mol. Phys.* **26**, 145 (1973); **27**, 279 (1974).
- [30] L. Wolniewicz and T. Orlikowski, *Mol. Phys.* **74**, 103 (1991).
- [31] L. Wolniewicz, *J. Chem. Phys.* **103**, 1792 (1995).
- [32] J. Liu, E. J. Salumbides, U. Hollenstein, J. C. J. Koelemeij, K. S. E. Eikema, W. Ubachs, and F. Merkt, *J. Chem. Phys.* **130**, 174306 (2009).
- [33] L. Wolniewicz, *J. Chem. Phys.* **99**, 1851 (1993).
- [34] P. Borrell, P. M. Guyon, and M. Glass-Maujean, *J. Chem. Phys.* **66**, 818 (1977).
- [35] J. Breton, P. M. Guyon, and M. Glass-Maujean, *Phys. Rev. A* **21**, 1909 (1980).
- [36] G. Herzberg and Ch. Jungen, *J. Chem. Phys.* **77**, 5876 (1982).
- [37] P. M. Dehmer and W. A. Chupka, *J. Chem. Phys.* **65**, 2243 (1976).
- [38] L. Wolniewicz, T. Orlikowski, and G. Staszewska, *J. Mol. Spectrosc.* **238**, 118 (2006).
- [39] Ch. Jungen and S. C. Ross, *Phys. Rev. A* **55**, 2503(R) (1997).
- [40] M. Glass-Maujean, J. Breton, and P. M. Guyon, *Phys. Rev. Lett.* **40**, 181 (1978).